Scholars Journal of Physics, Mathematics and Statistics

OPEN ACCESS

Abbreviated Key Title: Sch J Phys Math Stat
ISSN 2393-8056 (Print) | ISSN 2393-8064 (Online)
Journal homepage: https://saspublishers.com

Enhancing Perovskite Solar Cell Efficiency Via Tunable Ag Nanoparticle-Integrated SnO_2 Transport Layers: Mechanistic Insights and Air-Fabrication Approach

Hafiz Muhammad Leghari[1], Intazar Hussain Shah[2], Faisal Shahzad[3], Ihtisham Ul Haq[4], Mohammed Ateeq Mudassar[5], Faiza Ashfaq[6], Humaira Ghazal[7], Aleena Munawar[7], Samra Shehzadi[5], Waheed Zaman Khan[5*]

[1]Institute of Physics, The Islamia University of Bahawalpur, Pakistan
[2]Centre of Excellence in Solid State Physics, University of the Punjab, New Campus, Lahore, 54590, Pakistan
[3]Department of Physics, Riphah International University, Islamabad, Pakistan
[4]Department of Physics, Bacha Khan University, Charsadda, 24420, Khyber Pakhtunkhwa (KPK), Pakistan
[5]Department of Physics, Division of Science and Technology, University of Education, Lahore, Punjab 54770, Pakistan
[6]Department of Physics, University of Okara, Pakistan
[7]Department of Physics, University of the Punjab, Lahore, Punjab 54470, Pakistan

DOI: https://doi.org/10.36347/sjpms.2025.v12i07.002 | **Received:** 28.05.2025 | **Accepted:** 21.07.2025 | **Published:** 07.08.2025

***Corresponding author:** Waheed Zaman Khan
Department of Physics, Division of Science and Technology, University of Education, Lahore, Punjab 54770, Pakistan

Abstract | **Original Research Article**

Perovskite solar cells (PSCs) have evolved to become one of the most advantageous photovoltaic technologies with challenges on stability, charge transport and scalability; which have hindered them to attain a greater power output. This paper presents an assessment of the use of silver (Ag) nanoparticles in the SnO_2 electron transport layer (ETL) of CH 3NH 3PbI 3 -based PSCs in an attempt to improve the performance of the devices by increasing charge collection and the interface. There were two different fabrication techniques investigated including thermal evaporation and chemical synthesis. Thermally evaporated Ag nanoparticles showed lower efficiency as they increased the recombination whereas the chemically synthesized nanoparticles incorporated in SnO_2 could be tuned to improve the efficiency. Its best concentration (Ag:SnO_2 ratio of 2:1) produced a maximum Power conversion efficiency (PCE) of 14.3 26 0.3 wt-%, which is higher than the reference (13.4 26 0.7 wt-%) and beats previously reported values of air-processed, nanoparticle-integrated PSCs. UV-Vis and AFM analysis showed that Ag nanoparticles enabled quicker electron extraction (verified by lower PL lifetimes and lower series resistance) but also improved the recombination rates with the increased loadings. In confirmation of optimized device performance at medium Ag levels, both effective carrier life time and J-V behavior showed that the device performs best at medium Ag levels. This study shows that well-designed incorporation of Ag nanoparticles in SnO_2 ETLs can have a profound benefit in the performance of PSCs by transporting charges better but not losing low-temperature and air-compatible manufacturing methods, a scalable route to efficient and stable perovskite photovoltaics.

Keywords: Perovskite solar cells (PSCs), Silver nanoparticles (Ag NPs), Electron transport layer (ETL), Tin oxide (SnO_2), Power conversion efficiency (PCE), Charge transport.

1. INTRODUCTION

Over the past decade, the field of photovoltaics has witnessed a paradigm shift driven by the rapid emergence of halide perovskite-based solar cells (PSCs). Since their initial demonstration by Miyasaka *et al*. in 2009, where they achieved a modest efficiency of 3.8% in dye-sensitized solar cells using a perovskite absorber [1], the performance trajectory of PSCs has been nothing short of remarkable. As of 2023, certified power conversion efficiencies (PCEs) have soared to 26.1% [2], rivaling or even surpassing traditional silicon-based technologies. This meteoric rise is attributed to the unique optoelectronic properties of halide perovskites, including their high absorption coefficients [3], balanced electron and hole mobilities [4], long carrier diffusion lengths, and remarkable defect tolerance [5].

Despite this impressive progress, several technical barriers continue to hinder the commercial deployment of PSCs. One of the most pressing concerns is their sensitivity to environmental factors such as oxygen, moisture, ultraviolet (UV) radiation, and elevated temperatures, which severely affect both processing and long-term operational stability. Achieving high device performance typically requires stringent environmental control during fabrication—often necessitating gloveboxes or inert atmospheres—to prevent degradation of the perovskite layer. As a result, the power conversion efficiency under ambient conditions still lags, with most reports limited to ~20% [6]. In parallel, challenges related to scalability, material compatibility, and the availability of stable and cost-effective charge transport layers also persist [7,8].

In particular, the electron transport layer (ETL) plays a pivotal role in the overall device efficiency and stability. Although state-of-the-art devices often rely on doped ETLs such as spiro-OMeTAD or modified TiO_2 and SnO_2 systems, these dopants have been shown to induce degradation in the perovskite layer over time [9–12]. Hence, the development of low-cost, dopant-free, and stable transport layers remains a critical area of research for sustainable PSC technology.

Inspired by strategies established in organic photovoltaics (OPVs) and dye-sensitized solar cells (DSSCs), one promising approach involves the incorporation of metal nanoparticles (NPs) into charge transport layers to form composite structures. These nanocomposite architectures have demonstrated enhancements in device efficiencies ranging from 15% to 70% compared to baseline devices without nanoparticles [13]. The beneficial role of metallic nanoparticles—particularly those made from noble metals like gold or silver—has been extensively investigated in OPVs and DSSCs, but remains underexplored in PSCs, especially within specific ETLs such as SnO_2 [14–18].

SnO_2 is among the most promising electron transport materials due to its excellent electron mobility, wide band gap, low-temperature processability (~100 °C), and chemical compatibility with perovskites. However, the integration of metal nanoparticles into SnO_2 has not been previously reported in the context of PSCs, despite its potential to simultaneously improve light harvesting, interface engineering, and charge extraction.

To address this gap, the present study investigates for the first time the incorporation of silver (Ag) nanoparticles into SnO_2-based ETLs for methylammonium lead iodide ($CH_3NH_3PbI_3$ or $MAPbI_3$) perovskite solar cells. Ag is selected as the metallic additive due to its exceptional electrical conductivity, high plasmonic activity in the visible spectrum, and the relative ease with which it can be synthesized in controlled nanostructured forms [24]. In contrast to prior studies which primarily relied on a single nanoparticle fabrication route, this work explores two distinct methods—chemical synthesis and physical deposition via thermal evaporation—to gain a comprehensive understanding of how nanoparticle morphology, concentration, and distribution influence device performance.

The composite SnO_2:Ag ETLs fabricated here are systematically characterized and subsequently integrated into planar PSC devices processed entirely in ambient conditions. This fabrication strategy not only reduces manufacturing complexity and cost but also moves PSC technology closer to scalable industrial production. $CH_3NH_3PbI_3$ is deliberately chosen as the photoactive layer due to its well-characterized behavior, allowing a focused investigation into how the ETL modifications impact device metrics. While more complex multi-cation formulations may yield higher efficiencies, the use of a single-cation perovskite eliminates confounding variables and ensures that performance gains are attributable to the Ag nanoparticle-enhanced ETL.

Additionally, theoretical studies and computational insights have significantly contributed to the exploration of novel perovskite materials and architectures. Investigations into double perovskites and actinide-based systems have provided a deeper understanding of their electronic, optical, and thermoelectric properties, reinforcing the potential of perovskite-derived materials for sustainable energy applications [59,60]. In parallel, nanotechnology has emerged as a transformative tool in overcoming the challenges of efficiency, stability, and energy storage in perovskite systems [61]. Furthermore, efforts have been made to tailor the optoelectronic, magnetic, and transport properties of double perovskites to support next-generation photovoltaic and energy devices [62]. Addressing critical issues such as device stability and environmental sustainability has also become a focal point in recent research, helping to align PSCs with real-world deployment requirements [63].

Furthermore, this work seeks to clarify the mechanisms underlying efficiency improvements observed in nanocomposite-based PSCs—a topic that remains debated in the literature. Various enhancement mechanisms have been proposed: (1) increased surface roughness and interfacial area enabling better physical contact and charge extraction [20], (2) increased conductivity and directional charge transport facilitated by embedded metal nanoparticles [21], and (3) optical benefits such as light scattering or localized surface plasmon resonance (LSPR) leading to enhanced absorption [22]. The size-dependent behavior of Ag nanoparticles is particularly important—particles smaller than 40 nm exhibit LSPR, while larger ones act primarily as light scatterers. Notably, for LSPR to

effectively couple with the perovskite, the nanoparticles must be positioned within a few tens of nanometers of the absorber layer [19].

By utilizing a combination of experimental characterizations—including impedance spectroscopy, photoluminescence decay, UV–Vis spectroscopy, and atomic force microscopy—this study quantifies both the optical and electrical effects of Ag nanoparticle incorporation. It also identifies the optimal concentration regime where the competing phenomena of improved charge extraction and increased carrier recombination are balanced to maximize device efficiency.

Ultimately, this work not only introduces a novel SnO_2-based nanocomposite ETL for ambient-processed PSCs, but also contributes valuable insights into the plasmonic and electrical mechanisms that govern nanoparticle-induced performance modulation in perovskite solar cells.

2. EXPERIMENTAL METHODS

2.1. Synthesis of Silver Nanoparticles

To evaluate the effects of silver (Ag) nanoparticles on the electron transport layer (ETL) of perovskite solar cells, two distinct synthesis techniques were employed: physical deposition via thermal evaporation and wet-chemical reduction.

Thermal evaporation, a high-purity physical technique, was conducted using an Edwards Auto 306 metal evaporator operating under a high vacuum in the range of 6–8 × 10^{-6} mbar. Silver pellets (purity: 99.99%), sourced from the Kurt J. Lesker Company, were evaporated from a resistively heated tungsten boat at a controlled deposition rate of approximately 0.1 nm/s. This allowed precise tuning of film thickness between 0.25 nm and 13.9 nm. For Ag films exceeding the percolation threshold (~5 nm), which typically yield quasi-continuous layers, a post-deposition thermal annealing step was applied to promote nanoparticle reorganization and agglomeration into discrete islands. The annealing was carried out in ambient air using a quartz tube furnace for 20 minutes at temperatures ranging from 100 °C to 400 °C, following previously reported protocols [25,26].

In parallel, chemically synthesized Ag nanoparticles were prepared through a reduction-based aqueous route. A dilute solution of silver nitrate (0.002 M $AgNO_3$; Alfa Aesar) was reacted with an equal volume of freshly prepared sodium borohydride solution (0.001 M $NaBH_4$; Sigma-Aldrich) under constant stirring in deionized (DI) water. Upon reduction, the solution exhibited a yellow-brown hue characteristic of colloidal Ag nanoparticles. To enhance nanoparticle stability and prevent uncontrolled agglomeration, polyvinylpyrrolidone (PVP; MW = 10,000; Sigma-Aldrich) was added as a capping agent immediately following synthesis [27]. The resulting colloidal suspension was stored at 4 °C for later incorporation into the ETL matrix.

2.2. Fabrication of SnO_2:Ag Nanocomposite ETLs

Two distinct configurations were designed for integrating Ag nanoparticles into the SnO_2 electron transport layers:

(a) nanoparticles deposited beneath the SnO_2 layer, and

(b) nanoparticles embedded within the SnO_2 layer.

For physically deposited nanoparticles, the Ag layer was first thermally evaporated onto cleaned substrates as described in Section 2.1. Subsequently, a colloidal SnO_2 solution was spin-coated atop the Ag-modified substrate, encapsulating the nanoparticles between the substrate and the oxide matrix.

For the embedded configuration, Ag nanoparticles synthesized via the chemical method were blended directly with a commercial colloidal SnO_2 solution (15 wt% in DI water; Alfa Aesar). The SnO_2 precursor was diluted in DI water at a volumetric ratio of 1:4 (SnO_2:DI H_2O) to facilitate spin-coating. In the composite formulations, the aqueous Ag nanoparticle dispersion replaced part or all of the DI water used in the dilution, resulting in Ag/SnO_2 volumetric ratios of 1:1, 2:1, and 4:1. These mixed solutions were spin-coated at 2000 rpm for 30 seconds to form a uniform thin film and subsequently annealed at 100 °C for 30 minutes in air [28,29].

This dual-integration strategy enabled the comparison of different nanoparticle distributions and topologies, allowing insight into how nanoparticle position and interaction with the SnO_2 matrix affect charge extraction, recombination, and device performance.

2.3. Solar Cell Fabrication and Device Architecture

Perovskite solar cells were fabricated in a standard planar heterojunction architecture with the structure:
ITO/SnO_2:Ag/$MAPbI_3$/PTAA/Ag, as illustrated in Figure 1. All processing steps were carried out under ambient atmospheric conditions to assess real-world fabrication compatibility.

Substrate Preparation:

Commercial ITO-coated glass substrates (8-pixel design, 100 nm ITO thickness, 20 Ω/□ sheet resistance; Ossila Ltd.) were cleaned using a sequential ultrasonic bath protocol. The cleaning sequence included 10 minutes in 0.5% Hellmanex III (Hellma Analytics) solution in boiling DI water, followed by thorough rinsing in hot and room-temperature DI water. This was followed by 10 minutes of ultrasonication in acetone and then isopropanol (≥99.5%; Fisher Scientific). The substrates were then dried under nitrogen and treated

with oxygen plasma for 5–10 minutes to enhance surface wettability and remove residual organics.

ETL Deposition:

SnO_2 layers (pristine or nanocomposite) were deposited as detailed in Section 2.2.

Perovskite Layer Deposition:

Methylammonium lead iodide ($CH_3NH_3PbI_3$) perovskite was selected for the light-absorbing layer due to its well-studied performance profile. The CH_3NH_3I and PbI_2 precursors were synthesized in-house following previously published procedures [32,33]. The precursors were mixed in a 1:1 molar ratio in a solvent system of DMF:DMSO (4:1 by volume) to yield a 1.3 M perovskite solution. Spin coating was performed inside a fume hood at 3000 rpm for 20 seconds, with ethyl acetate (anhydrous, 99.8%; Sigma-Aldrich) added dropwise after 10 seconds as an antisolvent [31].

Following deposition, the films were immediately transferred to a low-vacuum chamber (~1.2 mbar) for 2 minutes to induce intermediate phase formation, which helps in enhancing film crystallinity. Subsequently, films were annealed at 100 °C for 1 minute to complete perovskite crystallization. This vacuum-assisted technique has been optimized to yield uniform, pinhole-free films with low surface roughness and enhanced grain boundary connectivity—crucial for devices processed entirely in ambient air.

Hole Transport Layer (HTL):

Poly(triarylamine) (PTAA; Ossila Ltd., MW = 28,422) was used as the hole-transport material due to its high ambient-process compatibility. A 15 mg/mL PTAA solution in anhydrous toluene was doped with two additives: lithium bis(trifluoromethylsulfonyl)imide (Li-TFSI; 170 mg/mL in acetonitrile) and 4-tert-butylpyridine (tBP; diluted 1:1 in acetonitrile). The dopant mixture was combined with the PTAA solution in a volume ratio of 1000:7.5:7.5 (PTAA:Li-TFSI:tBP). The final solution was statically deposited and spin-coated at 3000 rpm for 30 seconds, then annealed at 100 °C for 10 minutes [34–36].

Top Electrode and Contact Formation:

The top electrode was fabricated by thermally evaporating 110 nm of Ag using the same Edwards Auto 306 system described in Section 2.1. For electrochemical impedance spectroscopy (EIS) measurements, Au (99.99% purity; Agar Scientific) was used instead of Ag to minimize parasitic reactions, and was similarly deposited at 110 nm thickness via thermal evaporation.

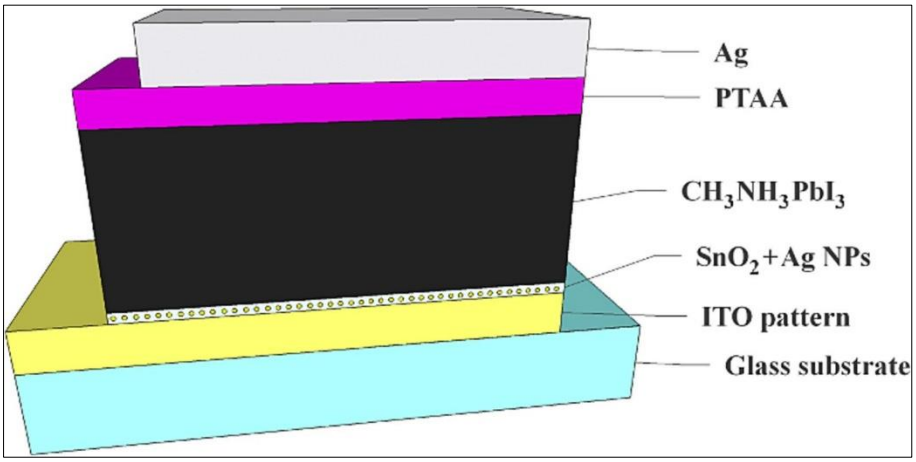

Fig. 1: Architecture of solar cells. Schematic representation of a solar cell, with layers: ITO (100 nm), SnO_2 (24.7 ± 0.1 nm), $CH_3NH_3PbI_3$ (373 ± 3 nm), PTAA (72.6 ± 0.2 nm), Ag (110 nm)

2.4. Characterization Techniques

A comprehensive suite of physical, optical, and electrical characterization techniques was employed to evaluate the morphology, conductivity, optical behavior, and device performance of the Ag nanoparticle-enhanced SnO_2 electron transport layers (ETLs) and the complete perovskite solar cell (PSC) devices.

Surface morphology was assessed using Atomic Force Microscopy (AFM), employing a Bruker Dimension Icon operating in ScanAsyst mode. Measurements were performed in ambient conditions in tapping mode, using silicon nitride ScanAsyst-Air probes with a nominal resonance frequency of 70 ± 25 kHz. This allowed for nanoscale surface topology visualization, root-mean-square (RMS) roughness estimation, and particle dispersion analysis.

UV–Visible absorbance spectra were recorded using a broadband deuterium–tungsten halogen light source covering the 250–830 nm range, coupled with an Ocean Optics USB 2000+ spectrometer. These measurements enabled detection of localized surface plasmon resonance (LSPR) peaks associated with silver nanoparticles and analysis of light-harvesting characteristics in the visible region.

Electrical conductivity of the transport layers was measured via a four-point probe method using a Keithley 2602A Source Meter. A voltage sweep from −1 V to +1 V was applied in 0.1 V increments, and current–voltage (I–V) characteristics were recorded to estimate sheet resistance and conductivity variations caused by nanoparticle incorporation.

Electrochemical Impedance Spectroscopy (EIS) was conducted using an IviumStat.h potentiostat integrated with a FRA/EIS module. Measurements were performed over a frequency range of 100 kHz to 100 mHz, applying a bias offset of 0.9 V. The data provided insights into charge transport, interfacial resistance, and recombination dynamics in the PSC devices.

Time-Resolved Photoluminescence (TRPL) measurements were carried out via the Time-Correlated Single Photon Counting (TCSPC) technique, employing a 510 nm excitation laser operating at 40 MHz with a fluence of 107 ± 1 μW. For each sample, the PL emission peak (~768 nm) was used as the detection wavelength to evaluate carrier recombination lifetimes and interfacial quenching behavior.

Photovoltaic performance of the fabricated devices was assessed under AM1.5G simulated sunlight using a calibrated Newport 92251A-1000 solar simulator equipped with a Xenon arc lamp. An aperture mask was applied to define the active area (2.365 ± 0.012 mm^2) of the solar cells. Prior to each measurement, the lamp intensity was adjusted to 1 sun using a certified reference cell to ensure consistency.

3. RESULTS AND DISCUSSION

3.1. Formation and Characterization of Ag Nanoparticles

3.1.1. Thermal Evaporation Method

Silver nanoparticles synthesized via thermal evaporation exhibited distinct growth regimes dependent on the initial film thickness and subsequent thermal treatment. As established in previous studies [37], thin Ag films (< 5 nm) deposited below the percolation threshold spontaneously formed discontinuous island-like structures. These nanoparticles exhibited pronounced LSPR behavior, evidenced by a distinct absorbance peak between 350–600 nm, and remained electrically insulating due to the lack of percolation pathways.

For thicker Ag films (> 5 nm), initial deposition led to the formation of quasi-continuous metallic films with flat optical spectra and measurable conductivity. However, upon post-deposition annealing in ambient air at temperatures between 100–400 °C for 20 minutes, these continuous layers underwent morphological rearrangement, transforming into hemispherical nanoparticles with strong, size-dependent plasmonic resonances centered between 430–500 nm.

The annealing temperature was tailored based on film thickness:

- 100 °C for ~1 nm films
- 200 °C for 2–5 nm films
- 300 °C for thicker films (10–13.9 nm)

This thermal transformation not only enhanced particle sphericity but also allowed precise tuning of nanoparticle size and interparticle spacing, which in turn modified the optical absorption profile of the layer. The ability to manipulate LSPR peaks by adjusting deposition and annealing parameters renders this approach highly suitable for optimizing light absorption within the device architecture [38].

3.1.2. Chemical Synthesis Method

In contrast, the chemically synthesized Ag nanoparticles were produced through rapid nucleation facilitated by a strong reducing agent ($NaBH_4$) acting on $AgNO_3$ in aqueous media. The use of a powerful reductant ensured the formation of ultrasmall nanoparticles with a narrow size distribution [27].

AFM analysis revealed spherical nanoparticles with an average radius of ~8.6 nm, closely corroborated by Nanoparticle Tracking Analysis (NTA), which indicated that approximately 50% of particles had diameters between 10–20 nm. The initial colloidal concentration, measured via NTA, was estimated to be ~9×10^{11} particles/mL. To increase the density of nanoparticles in the solution for embedding into SnO_2, the dispersion was subjected to two sequential high-speed centrifugations at 14,000 rpm for 60 minutes, concentrating the suspension by a factor of ~20×.

Optical absorption measurements of the colloidal suspension exhibited a sharp and well-defined plasmonic peak at 399.8 ± 0.8 nm, characteristic of small, monodisperse silver nanoparticles. These properties confirmed the suitability of the synthesized particles for integration into optoelectronic devices.

3.2. Integration of Ag Nanoparticles into SnO_2 Transport Layers

Building upon the two synthesis approaches, composite ETLs were fabricated by embedding the Ag nanoparticles within or beneath the SnO_2 matrix, and their structural and functional properties were systematically analyzed.

Optical Properties:

UV–Visible spectroscopy (Figure 2a) demonstrated distinct plasmonic absorbance peaks in samples containing thermally evaporated Ag nanoparticles. These exhibited well-resolved LSPR bands, indicating densely packed and closely spaced Ag nanostructures near the SnO_2 surface. In contrast, SnO_2 layers containing chemically synthesized Ag nanoparticles displayed no discernible absorption peaks

within the visible range, closely resembling the optical response of pristine SnO_2. This suggested a significantly lower particle concentration and larger interparticle separation in the chemically embedded layers.

Morphological Characteristics:

AFM imaging confirmed the trends observed in optical measurements. Thermally evaporated nanoparticles formed compact, contiguous arrangements with interparticle distances on the order of a few nanometers. Conversely, the chemically incorporated nanoparticles exhibited wider spacing—on the scale of tens of nanometers—due to the nature of spin-coating and limitations in colloidal concentration. Moreover, both composite systems displayed increased RMS surface roughness compared to bare SnO_2, which may enhance interfacial contact with the perovskite absorber.

Four-point probe measurements revealed that incorporation of Ag nanoparticles—regardless of synthesis method—led to a reduction in the electrical conductivity of the SnO_2 layers. This counterintuitive behavior can be rationalized by considering the difference in work function between Ag and SnO_2, which promotes electron transfer from the oxide matrix to the metal. This leads to local electron-depleted zones in the SnO_2 near the nanoparticle interfaces, effectively forming nano-scale Schottky junctions. These regions act as resistive barriers to charge transport, thereby reducing overall conductivity [39,40].

This trade-off highlights the dual nature of nanoparticle integration: while plasmonic and morphological advantages can enhance light harvesting and interface quality, electrical mismatches must be carefully managed to prevent losses in carrier transport.

Electrical Conductivity:

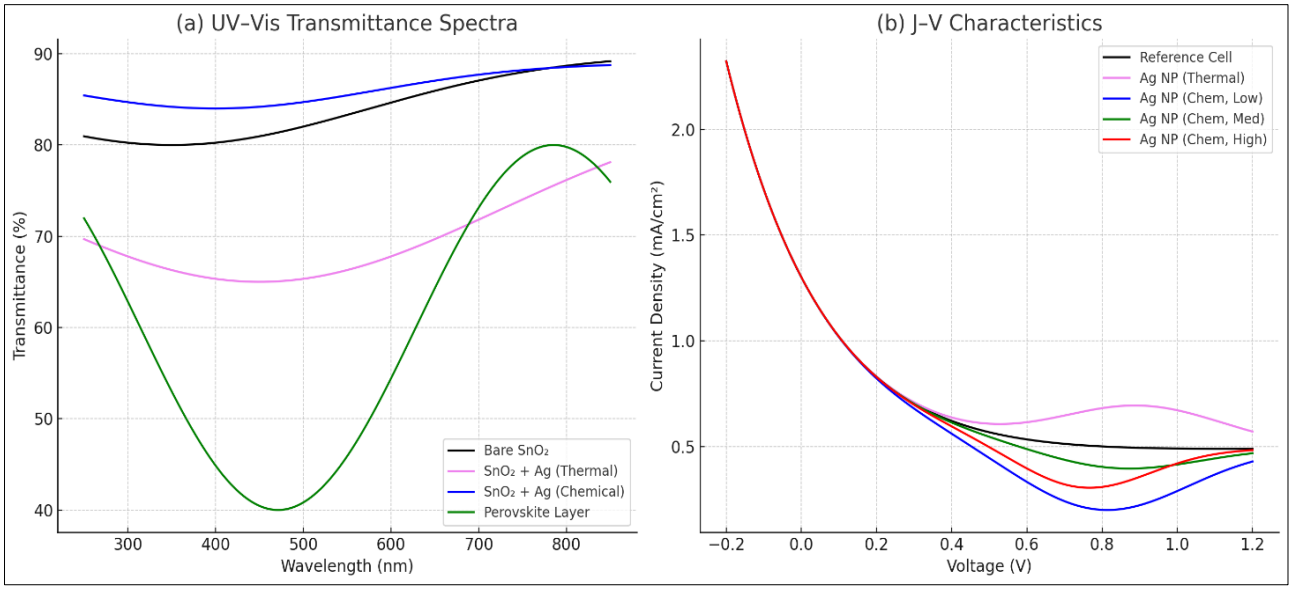

Fig. 2: (a) UV–Visible transmittance spectra of bare SnO_2, SnO_2 integrated with Ag nanoparticles via thermal evaporation and chemical synthesis, and the $CH_3NH_3PbI_3$ perovskite layer. The thermally evaporated Ag nanoparticles exhibit a pronounced plasmonic absorption dip, while the chemically synthesized NPs yield minimal optical modulation due to lower particle concentration

(b) Current density–voltage (J–V) characteristics of planar perovskite solar cells fabricated with different ETL configurations: the reference device (ITO/SnO_2/$CH_3NH_3PbI_3$/PTAA/Ag, black), a device with thermally evaporated Ag nanoparticles at the ITO/SnO_2 interface (violet), and devices incorporating chemically synthesized Ag nanoparticles into the SnO_2 layer at varying concentrations (blue, green, and red)

3.3. Integration of Ag Nanoparticles into the Transport Layers of Perovskite Solar Cells

To evaluate the influence of Ag nanoparticles on device performance, two integration strategies were implemented:

- Thermally evaporated Ag nanoparticles positioned at the interface between the indium tin oxide (ITO) substrate and the SnO_2 electron transport layer (ETL).
- Chemically synthesized Ag nanoparticles co-deposited within the SnO_2 matrix via solution processing.

Given that the average radii of the Ag nanoparticles synthesized by thermal evaporation (10–13 nm) and chemical reduction (8.6 nm) are both significantly smaller than the SnO_2 layer thickness (~25 nm), in both configurations the nanoparticles were fully embedded within the transport layer, minimizing

direct contact with the perovskite absorber and ensuring compatibility with standard planar device architectures.

3.3.1. Thermal Evaporation Method: Interface-Level Integration

When 1 nm thick Ag layers were thermally evaporated onto ITO and either left as-deposited or annealed at 100 °C and 200 °C, a marked decline in device efficiency was observed. Specifically, the power conversion efficiency (PCE) dropped by 54% to 80% compared to the reference cells without Ag nanoparticles. Figure 2b displays the J–V characteristics of the reference cell and the cell with the as-deposited 1 nm Ag layer, illustrating a significant reduction in short-circuit current density (J_{SC}), which is primarily responsible for the performance loss.

Several mechanisms likely contribute to this degradation:

- **Energy level misalignment**: The incorporation of metal nanoparticles at the ITO/SnO_2 interface may disturb the energetic alignment between the ETL and the perovskite, reducing efficient charge extraction.
- **Plasmonic competition**: Although Ag nanoparticles are capable of plasmonic enhancement, they can also compete for photon absorption. UV–Vis analysis (Figure 2a) showed only an ~11% reduction in optical transmission in the relevant spectral region—far less than the observed drop in PCE—implying that plasmonic parasitism is not the dominant cause.
- **Increased recombination**: The metal–semiconductor interface formed by Ag nanoparticles could serve as recombination centers, promoting non-radiative losses and reducing carrier lifetimes.

These findings suggest that while Ag nanoparticles possess favorable optical properties, direct placement at critical interfaces without concentration control may be detrimental to device performance.

3.3.2. Chemical Synthesis Method: Embedded Nanocomposite ETLs

To mitigate the issues associated with direct deposition, chemically synthesized Ag nanoparticles were mixed into the SnO_2 precursor solution, forming a uniformly embedded composite ETL. The Ag nanoparticle solution replaced deionized water in the SnO_2 dilution process at various volumetric ratios: 0:1 (pristine SnO_2), 1:1, 2:1, and 4:1.

Figure 2b compares the J–V curves of the reference and composite devices, and Table 1 summarizes the photovoltaic performance parameters—PCE, open-circuit voltage (V_{OC}), J_{SC}, fill factor (FF), shunt resistance (R_{SH}), and series resistance (R_S)—across all concentrations.

The highest efficiency, $14.3 \pm 0.3\%$, was achieved at the 2:1 ratio of Ag nanoparticle solution to SnO_2, corresponding to a relative improvement of 7% over the reference cell ($13.4 \pm 0.7\%$). This enhancement resulted primarily from:

- A modest increase in V_{OC} (~+1%), indicating improved interface passivation or reduced recombination;
- An 8% increase in FF, reflecting more efficient charge transport and extraction;
- A slight decrease in J_{SC}, potentially due to minor light scattering losses or non-ideal optical interference effects.

To further explore the effect of nanoparticle concentration, the Ag colloid was concentrated via additional centrifugation, reaching an equivalent dilution ratio of 64:1 (noted in Figure 2b, light blue curve). Interestingly, while V_{OC} continued to increase with concentration, both J_{SC} and FF decreased significantly, resulting in a net decline in PCE. This observation reinforces the non-monotonic relationship between nanoparticle loading and device performance: there exists an optimal concentration (~2:1), beyond which recombination or transport losses outweigh optical benefits.

3.3.3. Comparative Analysis and Literature Context

The contrasting outcomes between thermally and chemically integrated nanoparticles can be attributed primarily to nanoparticle concentration and dispersion. Thermal evaporation leads to high-density Ag layers near or beyond the percolation threshold, potentially inducing electrical shorts or severe interfacial recombination. In contrast, the colloidal chemical approach allows for precise, solution-based tuning of nanoparticle density within the SnO_2 network.

Our findings corroborate and extend previous studies involving plasmonic metal nanoparticles embedded in other oxide transport layers such as TiO_2 [14–16,41–45], Al_2O_3 [42,46], MgO [17], and VO_x [47]. Among the devices fabricated entirely in ambient conditions, the previous best efficiency was 13.85% for solar cells incorporating Au/SiO_2 core–shell nanoparticles in mesoporous TiO_2 [41]. By comparison, our $14.3 \pm 0.3\%$ device represents a record performance for nanostructure-enhanced planar PSCs fully processed in air using SnO_2-based ETLs.

Table 1. Photovoltaic parameters of ITO/SnO_2(+Ag NPs)/$CH_3NH_3PbI_3$/PTAA/Ag solar cells at varying Ag nanoparticle loadings. Both average values and best-performing device data are presented. Literature benchmarks for plasmonic solar cells fabricated under ambient conditions are provided for reference [41].

Ag NPs: SnO_2	PCE (%)	V_{OC} (V)	J_{SC} (mA/cm²)	FF (%)	R_{SH} (Ω·cm²)	R_S (Ω·cm²)
0:1 (Ref)	13.4 ± 0.7 / 14.41	1.01 ± 0.01 / 1.006	22.0 ± 0.4 / 22.63	60.2 ± 3.2 / 63.27	880 ± 650	9.4 ± 4.5
1:1	13.8 ± 0.6 / 14.64	1.01 ± 0.01 / 1.024	21.8 ± 0.5 / 22.38	62.7 ± 2.3 / 63.85	1100 ± 1400	6.6 ± 0.8
2:1	14.3 ± 0.3 / 14.87	1.02 ± 0.01 / 1.019	21.6 ± 0.3 / 21.87	65.1 ± 1.4 / 66.71	6600 ± 11000	6.2 ± 0.4
4:1	14.1 ± 0.8 / 15.02	1.02 ± 0.01 / 1.028	21.1 ± 1.0 / 21.59	65.1 ± 2.1 / 67.67	1500 ± 1900	7.1 ± 0.8
Ref. [41]	13.85 ± 0.45	0.995 ± 0.017	21.43 ± 1.01	64.3 ± 1.6	–	–

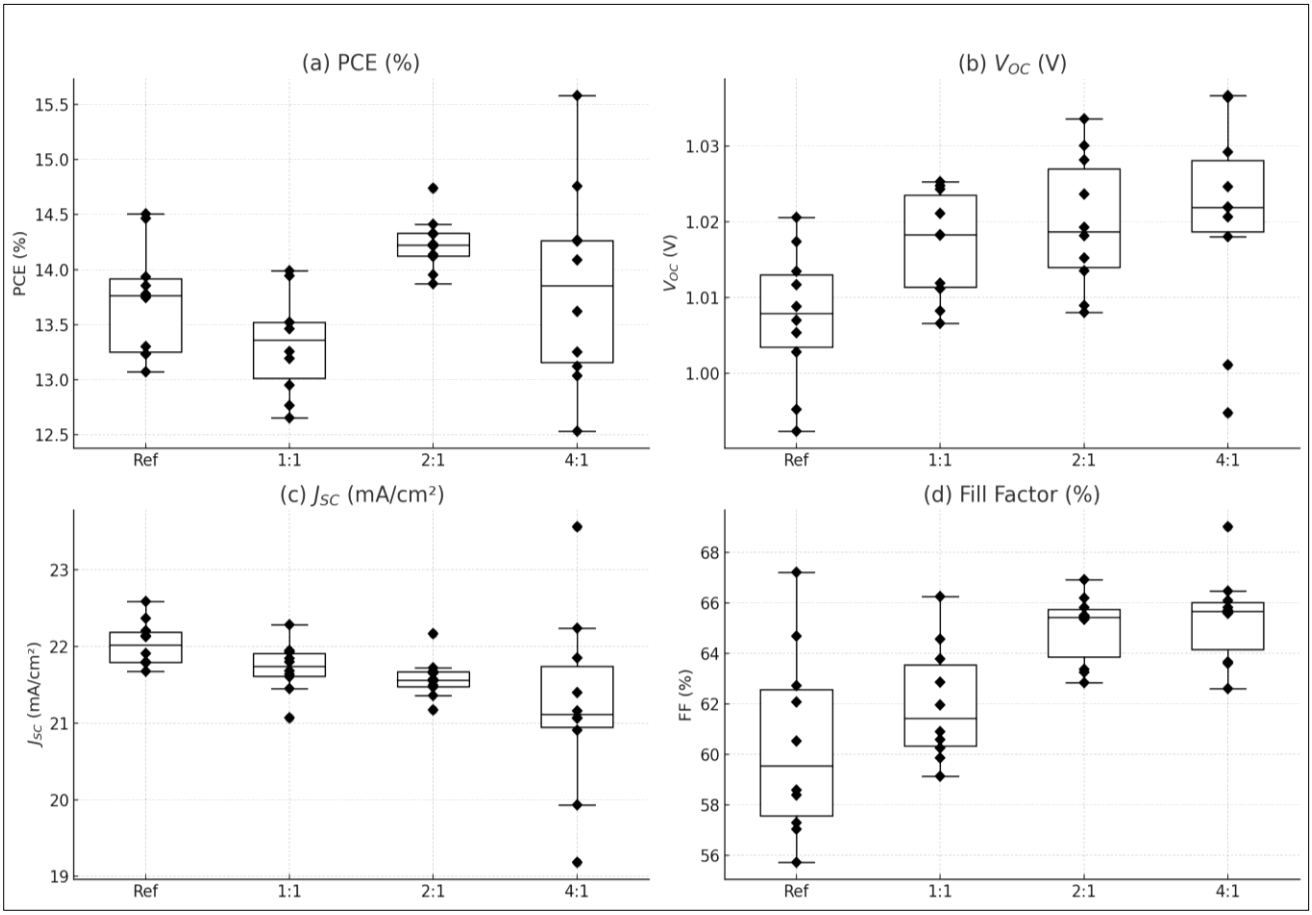

Fig. 3. Main Parameters of Solar Cells with Ag NP-SnO_2 Composite ETLs

Box plots with individual data points for:

- **(a) PCE (%)**: Power conversion efficiency increased at 2:1 concentration, but showed decline at 4:1 due to rising recombination and lowered J_{SC}.
- **(b) V_{OC} (V)**: Open-circuit voltage shows a consistent upward trend with increasing Ag NP content.
- **(c) J_{SC} (mA/cm²)**: Short-circuit current density decreased slightly with increasing NP concentration, indicating a balance between optical benefits and recombination losses.
- **(d) Fill Factor (%)**: FF peaked at 2:1 concentration, supporting the optimal charge extraction scenario.

3.4. Investigation of the Mechanism for Efficiency Improvement

To elucidate the origin of the observed enhancement in power conversion efficiency (PCE) upon incorporation of chemically synthesized Ag

nanoparticles into the SnO_2 electron transport layer (ETL), a comprehensive suite of characterization techniques was employed. These included UV–Visible (UV–Vis) spectroscopy, conductivity measurements under illumination, surface morphology via Atomic Force Microscopy (AFM), Electrochemical Impedance Spectroscopy (EIS), and Time-Resolved Photoluminescence (TRPL) using Time-Correlated Single Photon Counting (TCSPC).

3.4.1. Optical and Electrical Observations

As previously discussed, UV–Vis spectroscopy revealed no discernible localized surface plasmon resonance (LSPR) signatures in the composite layers containing chemically synthesized Ag nanoparticles. This absence of a plasmonic absorption peak is attributed to the relatively low concentration of nanoparticles and their broad spatial dispersion within the ~25 nm thick SnO_2 matrix. The dilution effect significantly diminishes the collective optical response typically associated with tightly packed metallic nanostructures.

To simulate operational conditions, conductivity measurements were repeated under 1-sun illumination. Interestingly, the composite SnO_2:Ag layers exhibited a reduced conductivity compared to pristine SnO_2, even when exposed to light. This suggests that the incorporation of Ag nanoparticles alters the electronic structure of the ETL in a manner that inhibits lateral charge transport, likely due to carrier trapping at the metal–semiconductor interfaces.

AFM analysis further showed an increase in RMS surface roughness from 1.181 nm (bare SnO_2) to 1.673 nm in the Ag nanoparticle-loaded layer. This enhanced roughness could improve the mechanical and electrical contact with the perovskite absorber, facilitating better interfacial adhesion and potentially aiding in electron extraction. However, this effect alone was insufficient to explain the observed improvements in device performance, prompting further investigation into recombination and transport phenomena.

3.4.2. Electrochemical Impedance Spectroscopy (EIS) Analysis

To probe interfacial dynamics and charge carrier behavior, EIS measurements were conducted on complete perovskite solar cells incorporating SnO_2:Ag composite layers with varying nanoparticle concentrations. The measurements were performed in the dark under a bias of 0.9 V, and the resulting Nyquist plots (imaginary vs. real impedance) are shown in Figure 4a.

The experimental data were modeled using an equivalent electrical circuit consisting of a series resistor (R_1) in series with a parallel RC element (R_2 and C_2), as shown in the inset of Figure 4a. In one case, an additional parallel RC pair was introduced to accurately capture the impedance response. The extracted values of R_1, R_2, and C_2 are summarized in Table 2.

Impedance responses at different frequency domains are typically attributed to distinct physical processes:

- **High frequencies (≥100 kHz):** Fast processes such as charge transport and extraction.
- **Mid frequencies (10–100 kHz):** Non-radiative and radiative recombination events.
- **Low frequencies (100–1000 Hz):** Slow processes like ion migration and trap-assisted charge accumulation [48–52].

In this study, the dominant arc features appeared in the intermediate frequency range, suggesting that recombination processes were the major contributors to the impedance signal. The characteristic time constant, $\tau = R \times C$, derived from R_2 and C_2, is plotted in Figure 4b as a function of Ag nanoparticle concentration.

A clear trend was observed: τ decreased with increasing Ag NP concentration, indicating that charge recombination occurred more rapidly. This suggests that Ag nanoparticles may act as recombination centers, facilitating electron–hole recombination near the perovskite/ETL interface. This mechanism explains the slight drop in short-circuit current density (J_{SC}) observed in Figure 3c at higher NP loadings and supports the interpretation that excessive nanoparticle concentration can be detrimental to performance.

3.4.3. Series Resistance and Conductivity Anisotropy

Interestingly, EIS analysis also revealed that the series resistance R_1 decreased upon nanoparticle incorporation. At first glance, this appears contradictory to the 4-point probe measurements, which showed reduced conductivity in the nanoparticle-loaded layers.

This apparent inconsistency is reconciled by considering the anisotropic nature of electrical transport in the composite ETL:

- 4-point probe measurements assess in-plane (lateral) conductivity, where nanoparticle-induced electron depletion zones lower the effective carrier density and increase resistance.
- In contrast, EIS measurements probe out-of-plane (vertical) transport across the device stack. In this configuration, Ag nanoparticles may form percolation-like channels that facilitate direct electron pathways from the perovskite absorber into the ITO contact, reducing the effective vertical resistance.

Thus, while Ag nanoparticles impede lateral conductivity within the ETL plane, they simultaneously enhance vertical electron extraction, contributing positively to fill factor and open-circuit voltage—up to an optimal concentration.

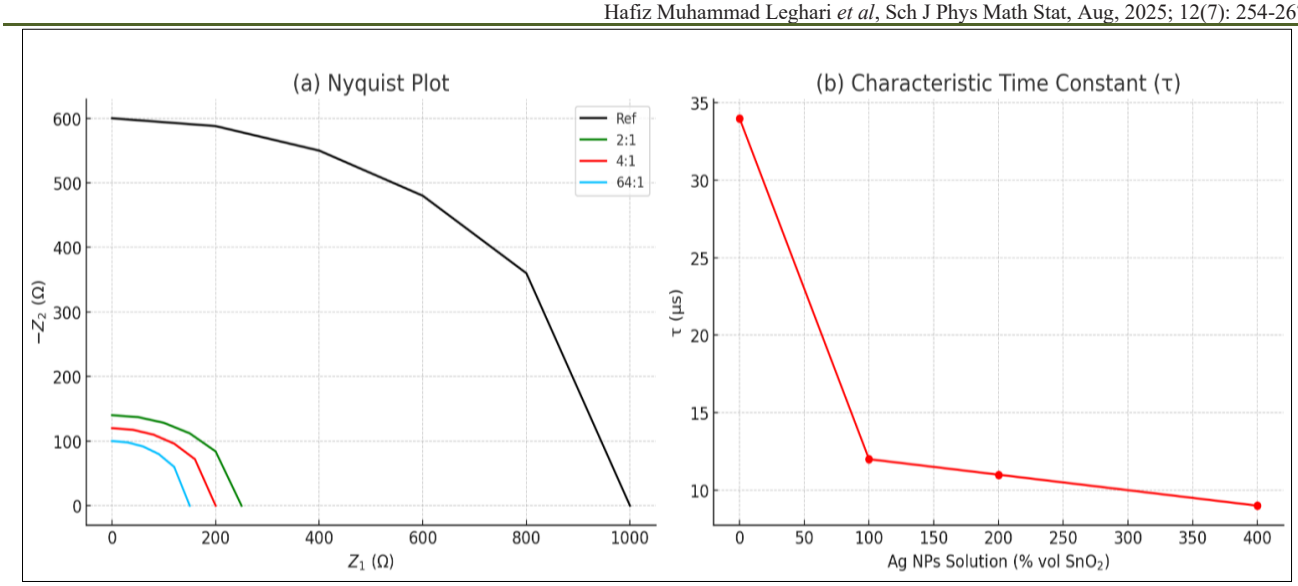

Fig. 4. Electrochemical Impedance Spectroscopy (EIS) Results

(a) Nyquist plot showing the real (Z_1) vs. negative imaginary ($-Z_2$) components of impedance for eight perovskite solar cells with SnO_2 electron transport layers incorporating different Ag nanoparticle concentrations. The EIS measurements were conducted at 0.9 V in dark conditions. Each arc corresponds to the characteristic recombination response, and solid lines represent fitted data using the equivalent circuit shown in the inset. **(b)** Extracted characteristic time constants τ = R·C for intermediate frequency arcs, plotted as a function of Ag nanoparticle content (as % volume of SnO_2). The decrease in τ indicates faster recombination rates at higher nanoparticle loadings.

All measurements were performed at 0.9 V under dark conditions. The fits used either a single (R + RC) or double (R + RC + RC) equivalent circuit model, as indicated. R_1 represents the series resistance, R_2 and C_2 define the main RC arc, and R_3 and C_3 are used when a secondary arc is present.

Table 2: Electrochemical impedance spectroscopy (EIS) fitting parameters for perovskite solar cells with varying Ag nanoparticle concentrations

Ag NPs : SnO_2	Equivalent Circuit	R_1 (Ω)	R_2 (Ω)	C_2 (nF)	R_3 (Ω)	C_3 (nF)
0 : 1 (Ref I)	R + RC	42.2 ± 0.6	799 ± 3	39.7 ± 0.3	–	–
0 : 1 (Ref II)	R + RC	82.2 ± 1.9	1050 ± 20	22.3 ± 0.2	–	–
1 : 1	R + RC + RC	40.5 ± 1.4	193 ± 7	61.0 ± 1.6	210 ± 11	705 ± 71
2 : 1 (I)	R + RC	33.4 ± 0.7	280 ± 2	43.9 ± 0.5	–	–
2 : 1 (II)	R + RC	34.2 ± 0.8	266 ± 3	44.7 ± 0.5	–	–
4 : 1 (I)	R + RC	37.8 ± 0.9	197 ± 2	44.4 ± 0.7	–	–
4 : 1 (II)	R + RC	35.7 ± 0.5	185 ± 1	45.8 ± 0.4	–	–

3.5. Photoluminescence Dynamics via Time-Correlated Single Photon Counting (TCSPC)

To further investigate the role of Ag nanoparticles on carrier dynamics within the transport layer, Time-Correlated Single Photon Counting (TCSPC) measurements were conducted on electron-only devices with the architecture:

glass/SnO_2(+Ag nanoparticles)/$CH_3NH_3PbI_3$/ encapsulation glass. These devices isolate electron extraction behavior by eliminating hole-transport contributions.

The photoluminescence (PL) decay spectra, normalized and plotted in Figure 5a, were fitted using a double-exponential decay model:

$$I(t) = I_0 + A_1 e^{-t/\tau_1} + A_2 e^{-t/\tau_2} I(t)$$

Here, τ_1 and τ_2 correspond to fast and slow decay components respectively, which in the literature have been ascribed to:

- Bimolecular vs. free-carrier recombination mechanisms [53]
- Surface vs. bulk recombination [54, 55]
- Transitions from multiple energy states within the perovskite [56]

The fitted parameters, including the pre-exponential weights (A_1, A_2), decay constants (τ_1, τ_2), and the effective lifetime τ_{EFF} defined by:

$$\frac{1}{\tau_{EFF}} = \frac{1}{\tau_1} + \frac{1}{\tau_2}$$

are reported in **Table 3** and visualized in **Figure 5b**.

3.5.1. Interpretation of TCSPC Results

Analysis of the decay amplitudes revealed a key trend:

- For devices incorporating Ag nanoparticles, **A_1** (the short-time component) is dominant, indicating accelerated initial

carrier extraction.

- In contrast, the reference SnO_2 device exhibits a more balanced decay profile, suggesting a greater degree of recombination-limited transport.

The effective lifetimes τ_{EFF} varied significantly with nanoparticle concentration. The reference sample showed τ_{EFF} = 1.223 ± 0.013 ns, whereas the 2:1 Ag NPs:SnO_2 sample exhibited the shortest τ_{EFF} at 0.744 ± 0.007 ns, indicating faster electron extraction from the perovskite layer into the transport layer.

This improvement in charge extraction is further corroborated by EIS results, which revealed a minimum in series resistance (R_1) at the same 2:1 concentration, supporting a consistent interpretation across techniques.

However, faster extraction comes with a trade-off:

EIS analyses showed that higher concentrations of Ag NPs also enhanced recombination rates, decreasing J_{SC} and, at excessive concentrations, undermining device performance. Thus, while Ag nanoparticles facilitate carrier extraction, they can also act as recombination centers when overused.

The optimal balance was observed at the 2:1 Ag NPs:SnO_2 ratio, where the devices achieved a maximum PCE of $14.3 \pm 0.3\%$, surpassing the previously reported best performance for nanoparticle-enhanced air-processed devices (13.8%) [41].

By contrast, devices incorporating thermally evaporated Ag nanoparticles suffered from excessive recombination due to overconcentration at the interface, further validating the importance of concentration control and uniform dispersion.

Table 3: Fitted parameters of photoluminescence decay curves from TCSPC measurements, modeled using a bi-exponential function. τ_{EFF} is calculated from τ_1 and τ_2 to reflect the aggregate charge extraction behavior

Ag NPs : SnO_2	I_0 (counts)	A_1 (counts)	τ_1 (ns)	A_2 (counts)	τ_2 (ns)	τ_{EFF} (ns)
0:1 (Ref)	642 ± 3	9,520 ± 50	1.536 ± 0.010	9,770 ± 60	6.004 ± 0.024	**1.223 ± 0.013**
1:1	1,012 ± 8	67,200 ± 100	0.889 ± 0.003	41,900 ± 100	4.553 ± 0.013	**0.744 ± 0.005**
2:1	10,260 ± 70	454,800 ± 900	0.864 ± 0.003	139,200 ± 900	5.352 ± 0.031	**0.744 ± 0.007**
4:1	1,053 ± 7	17,450 ± 50	1.152 ± 0.006	11,170 ± 40	8.197 ± 0.038	**1.010 ± 0.010**

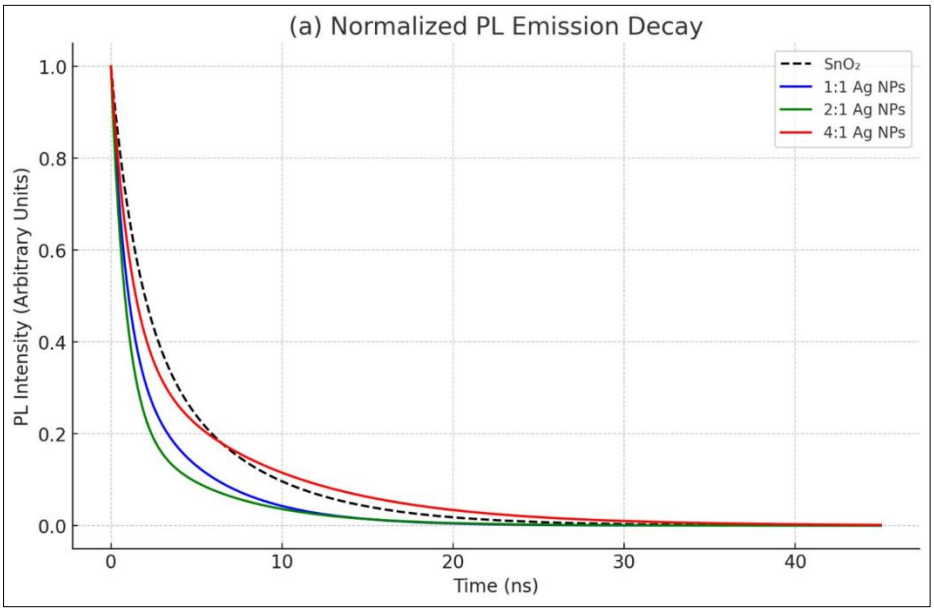

Fig. 5: (a) Normalized PL Intensity Decay

This plot shows the normalized photoluminescence (PL) intensity decay for devices with varying concentrations of Ag nanoparticles in the SnO_2 layer. The decay curves for different concentrations of Ag NPs (0:1, 1:1, 2:1, 4:1) were fitted with a double-exponential model, revealing differences in recombination dynamics.

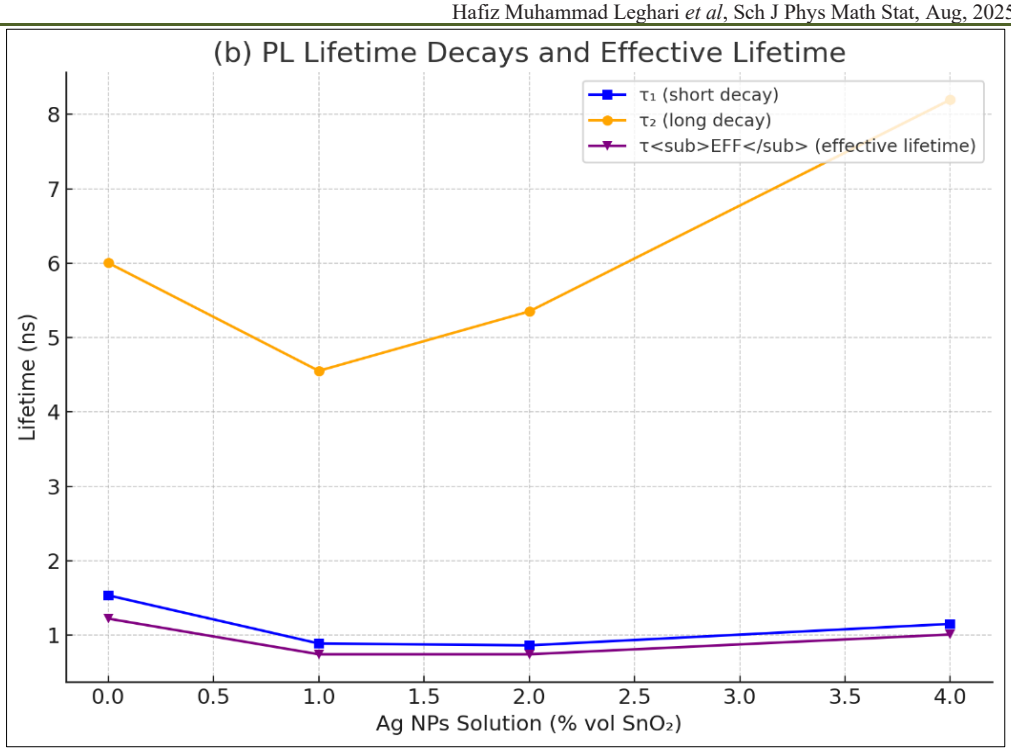

Fig. 5. (b) PL Lifetime Decays and Effective Lifetime

This plot compares the PL decay lifetimes (τ_1 and τ_2) for the short and long decay components, and the effective lifetime (τ_{EFF}), as a function of Ag nanoparticle concentration. It demonstrates how the addition of Ag NPs accelerates electron extraction, with τ_1 decreasing slightly and τ_2 increasing at higher nanoparticle concentrations, resulting in faster charge carrier extraction but also promoting recombination.

4. CONCLUSIONS

This study presents a comprehensive investigation into the incorporation of metal nanoparticles into the electron transport layer (ETL) of perovskite solar cells. The work demonstrates the synthesis and optimization of nanoparticles via both chemical and physical methods, followed by their integration into SnO_2-based transport layers.

The effects of these nanoparticles on the performance of perovskite solar cells were carefully examined. While thermally evaporated nanoparticles resulted in a decrease in power conversion efficiency (PCE), nanoparticles synthesized chemically and co-deposited with SnO_2 enhanced the PCE by +7%. This improvement provides a valuable solution to the ongoing debate in the literature regarding the mechanisms underlying these efficiency enhancements.

The detailed analysis presented here suggests that, while electrochemical impedance spectroscopy (EIS) revealed increased recombination rates with higher nanoparticle concentrations, photoluminescence (PL) measurements indicated a decrease in the charge transport lifetime from 1.223 ± 0.013 ns to 0.744 ± 0.007 ns after the integration of Ag nanoparticles into SnO_2. This reduction in lifetime can be interpreted as enhanced charge transfer from the perovskite layer into the electrode, thus facilitating faster charge extraction and ultimately leading to a higher PCE. The balance between charge extraction and recombination effects leads to an optimal nanoparticle concentration that maximizes performance. The chemical synthesis of Ag nanoparticles allowed for more precise control over their concentration, making it possible to achieve this optimal concentration, whereas thermally evaporated nanoparticles were limited to concentrations above the optimal range.

This work is pioneering in its approach, being the first to apply metal nanoparticles in SnO_2, one of the most efficient electron transport layers (ETLs) for perovskite solar cells. Moreover, the solar cells in this study represent some of the first devices to be fabricated entirely in air while incorporating a composite metal nanoparticle/oxide electron transport layer. With a PCE of 14.3 ± 0.3%, these devices set a new benchmark for the material system, surpassing previously reported efficiencies for air-processed perovskite solar cells.

In conclusion, this research not only provides a method for improving the efficiency of perovskite solar cells but also simplifies the fabrication process, eliminating the need for expensive control of the processing environment. Furthermore, the mechanisms explored in this study offer deeper insights into how nanoparticles enhance device performance. The protocols for synthesizing, comparing, and integrating composite transport layers established in this work are

versatile and can be applied to a range of perovskite solar cells with varying compositions, or even extended to other fields, such as LEDs, field-effect transistors (FETs), and fuel cells.

REFERENCES

1. Kojima, A.; Teshima, K.; Shirai, Y.; Miyasaka, T. *J. Am. Chem. Soc.* 2009, *131*, 6050–6051.
2. National Renewable Energy Laboratory. *Best Research-Cell Efficiency Chart*, accessed 2025-07-13. https://www.nrel.gov/pv/assets/images/efficiency-chart.png
3. Park, N. G. *Mater. Today* 2015, *18*, 65–72.
4. Giorgi, G.; Yamashita, K. *J. Mater. Chem. A* 2015, *3*, 8981–8991.
5. Luo, S.; Daoud, W. A. *J. Mater. Chem. A* 2015, *3*, 8992–9010.
6. Krishna, B. G.; Ghosh, D. S.; Tiwari, S. *Sol. Energy* 2021, *224*, 1369–1395.
7. Niu, G.; Guo, X.; Wang, L. *J. Mater. Chem. A* 2015, *3*, 8970–8980.
8. Calió, L.; Kazim, S.; Grätzel, M.; Ahmad, S. *Angew. Chem. Int. Ed.* 2016, *55*, 14522–14545.
9. Song, Z.; Liu, J.; Wang, G.; Zuo, W.; Liao, C.; Mei, J. *ChemPhysChem* 2017, *18*, 3030–3038.
10. Petrus, M. L.; Sirtl, M. T.; Closs, A. C.; Bein, T.; Docampo, P. *Mol. Syst. Des. Eng.* 2018, *3*, 734–740.
11. Petrus, M. L.; Bein, T.; Dingemans, T. J.; Docampo, P. *J. Mater. Chem. A* 2015, *3*, 12159–12162.
12. Valero, S.; Collavini, S.; Völker, S. F.; Saliba, M.; Tress, W. R.; Zakeeruddin, S. M.; Grätzel, M.; Delgado, J. L. *Macromolecules* 2019, *52*, 2243–2254.
13. Stavytska-Barba, M.; Salvador, M.; Kulkarni, A.; Ginger, D. S.; Kelley, A. M. *J. Phys. Chem. C* 2011, *115*, 20788–20794.
14. Lu, Z.; Pan, X.; Ma, Y.; Li, Y.; Zheng, L.; Zhang, D.; Xu, Q.; Chen, Z.; Wang, S.; Qu, B.; Liu, F.; Huang, Y.; Xiao, L.; Gong, Q. *RSC Adv.* 2015, *5*, 11175–11179.
15. Liu, Y.; Lang, F.; Dittrich, T.; Steigert, A.; Fischer, C. H.; Köhler, T.; Plate, P.; Rappich, J.; Lux-Steiner, M. C.; Schmid, M. *RSC Adv.* 2017, *7*, 1206–1214.
16. Yuan, Z.; Wu, Z.; Bai, S.; Xia, Z.; Xu, W.; Song, T.; Wu, H.; Xu, L.; Si, J.; Jin, Y.; Sun, B. *Adv. Energy Mater.* 2015, *5*, 1500038.
17. Zhang, C.; Luo, Q.; Shi, J.; Yue, L.; Wang, Z.; Chen, X.; Huang, S. *Nanoscale* 2017, *9*, 2852–2864.
18. Siavash, R.; Moakhar, R.; Gholipour, S.; Masudy-Panah, S.; Seza, A.; Mehdikhani, A.; Riahi-Noori, N.; Tafazoli, S.; Timasi, N.; Lim, Y. F.; Saliba, M. *Adv. Sci.* 2020, *7*, 2001019.
19. Gu, M.; Ouyang, Z.; Jia, B.; Stokes, N.; Chen, X.; Fahim, N.; Li, X.; Ventura, M. J.; Shi, Z. *Nanophotonics* 2012, *1*, 235–248.
20. Woo, S.; Jeong, J.; Lyu, H.; Han, Y.; Kim, Y. *Nanoscale Res. Lett.* 2012, *7*, 641.
21. Li, X.; Deng, Z.; Yin, Y.; Zhu, L.; Xu, D.; Wang, Y.; Teng, F. *J. Mater. Sci.: Mater. Electron.* 2014, *25*, 140–145.
22. Stratakis, E.; Kymakis, E. *Mater. Today* 2013, *16*, 133–146.
23. Min, H.; Lee, D. Y.; Kim, J.; Kim, G.; Lee, K. S.; Kim, J.; Paik, M. J.; Kim, Y. K.; Kim, K. S.; Kim, M. G.; Shin, T. J.; Seok, S. I. *Nature* 2021, *598*, 444–450.
24. Rycenga, M.; Cobley, C. M.; Zeng, J.; Li, W.; Moran, C. H.; Zhang, Q.; Qin, D.; Xia, Y. *Chem. Rev.* 2011, *111*, 3669–3712.
25. Kumar, A.; Rani, S.; Rana, N. K.; Samantaray, M. R.; Chander, N.; Ghosh, D. S. *Sol. Energy* 2022, *244*, 457–464.
26. Rani, S.; Kumar, A.; Ghosh, D. S. *Mater. Today: Proc.* In Press, *2025*.
27. Mulfinger, L.; Solomon, S. D.; Bahadory, M.; Jeyarajasingam, A. V.; Rutkowsky, S. A.; Boritz, C. *J. Chem. Educ.* 2007, *84*, 322–322.
28. Jiang, Q.; Zhao, Y.; Zhang, X.; Yang, X.; Chen, Y.; Chu, Z.; Ye, Q.; Li, X.; Yin, Z.; You, J. *Nat. Photonics* 2019, *13*, 460–466.
29. Jiang, Q.; Zhang, L.; Wang, H.; Yang, X.; Meng, J.; Liu, H.; Yin, Z.; Wu, J.; Zhang, X.; You, J. *Nat. Energy* 2016, *2*,1.
30. Jeon, N. J.; Noh, J. H.; Kim, Y. C.; Yang, W. S.; Ryu, S.; Seok, S. I. *Nat. Mater.* 2014, *13*, 897–903.
31. Troughton, J.; Hooper, K.; Watson, T. M. *Nano Energy* 2017, *39*, 60–68.
32. Stamplecoskie, K. G.; Manser, J. S.; Kamat, P. V. *Energy Environ. Sci.* 2015, *8*, 208–215.
33. Tsevas, K.; Smith, J. A.; Kumar, V.; Rodenburg, C.; Fakis, M.; Mohd Yusoff, A. R. B.; Vasilopoulou, M.; Lidzey, D. G.; Nazeeruddin, M. K.; Dunbar, A. D. *Chem. Mater.* 2021, *33*, 554–566.
34. Heo, J. H.; Lee, M. H.; Han, H. J.; Patil, B. R.; Yu, J. S.; Im, S. H. *J. Mater. Chem. A* 2016, *4*, 1572–1578.
35. Heo, J. H.; Han, H. J.; Kim, D.; Ahn, T. K.; Im, S. H. *Energy Environ. Sci.* 2015, *8*, 1602–1608.
36. Ryu, S.; Seo, J.; Shin, S. S.; Kim, Y. C.; Jeon, N. J.; Noh, J. H.; Seok, S. I. *J. Mater. Chem. A* 2015, *3*, 3271–3275.
37. Bastianini, F.; Dunbar, A. In *14th Photovoltaic Science, Applications & Technology Conf.*, PVSAT-14, 2018; pp 101–104.
38. Barreca, D.; Gasparotto, A.; Tondello, E.; Bruno, G.; Losurdo, M. *J. Appl. Phys.* 2004, *96*, 1655–1665.
39. Mohamedkhair, A. K.; Drmosh, Q. A.; Yamani, Z. H. *Front. Mater.* 2019, *6*,1.
40. Kolmakov, A.; Klenov, D. O.; Lilach, Y.; Stemmer, S.; Moskovits, M. *Nano Lett.* 2005, *5*, 667–673.
41. Qi, F.; Wang, C.; Cheng, N.; Liu, P.; Xiao, Y.; Li, F.; Sun, X.; Liu, W.; Guo, S.; Zhao, X. Z. *Electrochim. Acta* 2018, *282*, 10–15.
42. Zhang, W.; Saliba, M.; Stranks, S. D.; Sun, Y.; Shi, X.; Wiesner, U.; Snaith, H. J. *Nano Lett.* 2013, *13*, 4505–4510.

43. Abate, S. Y.; Wu, W. T.; Pola, S.; Tao, Y. T. *RSC Adv.* 2018, *8*, 7847–7854.
44. Wang, B.; Zhu, X.; Li, S.; Chen, M.; Lu, H.; Yang, Y. *Nanomaterials* 2018, *8*, 486–486.
45. Du, J.; Zhang, Y.; Yang, M.; Han, D.; Fan, L.; Sui, Y.; Yang, J.; Yang, L.; Wang, F. *ACS Appl. Mater. Interfaces* 2020, *12*, 41446–41453.
46. Saliba, M.; Zhang, W.; Burlakov, V. M.; Stranks, S. D.; Sun, Y.; Ball, J. M.; Johnston, M. B.; Goriely, A.; Wiesner, U.; Snaith, H. J. *Adv. Funct. Mater.* 2015, *25*, 5038–5046. Dong, H.; Lei, T.; Yuan, F.; Xu, J.; Niu, Y.; Jiao, B.; Zhang, Z.; Ding, D.; Hou, X.; Wu, Z. *Org. Electron.* 2018, *60*, 1–8.
47. Dong, H.; Lei, T.; Yuan, F.; Xu, J.; Niu, Y.; Jiao, B.; Zhang, Z.; Ding, D.; Hou, X.; Wu, Z. *Org. Electron.* 2018, *60*, 1–8.
48. Ng, C. H.; Lim, H. N.; Hayase, S.; Zainal, Z.; Huang, N. M. *Renew. Sustain. Energy Rev.* 2018, *90*, 248–274.
49. Ali, S.; Chang, S.; Imran, M.; Shi, Q.; Chen, Y.; Zhong, H. *Phys. Status Solidi RRL* 2019, *13*, 1900095.
50. Wang, H.; Guerrero, A.; Bou, A.; Al-Mayouf, A. M.; Bisquert, J. *Energy Environ. Sci.* 2019, *12*, 2054–2079.
51. Lopez-Varo, P.; Jiménez-Tejada, J. A.; García-Rosell, M.; Ravishankar, S.; Garcia-Belmonte, G.; Bisquert, J.; Almora, O. *Adv. Energy Mater.* 2018, *8*, 1702772.
52. Todinova, A.; Contreras-Bernal, L.; Salado, M.; Ahmad, S.; Morillo, N.; Idígoras, J.; Anta, J. J. *ChemElectroChem* 2017, *4*, 2891–2901.
53. Chen, Q.; Zhou, H.; Song, T. B.; Luo, S.; Hong, Z.; Duan, H. S.; Dou, L.; Liu, Y.; Yang, Y. *Nano Lett.* 2014, *14*, 4158–4163.
54. Staub, F.; Hempel, H.; Hebig, J. C.; Mock, J.; Paetzold, U. W.; Rau, U.; Unold, T.; Kirchartz, T. *Phys. Rev. Appl.* 2016, *6*, 044017.
55. Chen, P.; Bai, Y.; Wang, S.; Lyu, M.; Yun, J. H.; Wang, L. *Adv. Funct. Mater.* 2018, *28*, 1706923.
56. Chen, Y.; Wang, T.; Li, Z.; Li, H.; Ye, T.; Wetzel, C.; Li, H.; Shi, S. F. *Sci. Rep.* 2018, *8*, 3791.
57. Hu, X.; Wang, X.; Fan, P.; Li, Y.; Zhang, X.; Liu, Q.; Zheng, W.; Xu, G.; Wang, X.; Zhu, X.; Pan, A. *Nano Lett.* 2018, *18*, 3024–3031.
58. Atwater, H. A.; Polman, A. *Nat. Mater.* 2010, *9*, 205–213.
59. Tabassam, M. N.; Shahzad, A.; Almunyif, A. A.; Ali, S.; Murtaza, S.; Shahid, M. *J. Phys. Chem. Solids* 2025, *204*, 112770.
60. Nazar, M.; Tabassam, M. N.; Irfan, A.; Liaqat, M.; Ameen, M.; Chaudhary, H. M.; Murad, K.; Alam, S.; Sohaib, M.; Khan, W. Z. *Scholars J. Eng. Technol.* 2025, *13*(4), Article 002. https://doi.org/10.36347/sjet.2025.v13i04.002
61. Malik, A.; Liaqat, M.; Rahman, M. U.; Shafique, A. Y.; Haseeb, M.; Ahmad, S.; Kanwal, R.; Ramzan, M.; Yasmin, R.; Khan, W. Z. *Glob. Sci. Acad. Res. J. Multidiscip. Stud.* 2025, *4*(2), 68–89. https://doi.org/10.5281/zenodo.14913631
62. Liaqat, M.; Yasmin, R.; Rahman, M. U.; Tabassam, M. N.; Shahzad, A.; Ahmad, N.; Rafiq, M. N.; Khan, W. Z. *Glob. Sci. Acad. Res. J. Multidiscip. Stud.* 2025, *4*(1), 85. https://doi.org/10.5281/zenodo.14770877
63. Nazar, M.; Younis, B.; Akbar, H.; Ahmad, S.; Rustam, R.; Akram, I.; Munir, F. *Dialogue Soc. Sci. Rev.* 2024, *2*(4), 395–422.